Sensitivity of precipitation formation to secondary ice production in winter orographic mixed-phase clouds

Zane Dedekind[1], Annika Lauber[1], Sylvaine Ferrachat[1], and Ulrike Lohmann[1]

[1]Institute of Atmospheric and Climate Science, ETH Zurich, Switzerland

Correspondence: Zane Dedekind (zane.dedekind@env.ethz.ch) and Ulrike Lohmann (ulrike.lohmann@env.ethz.ch)

Abstract. The discrepancy between the observed concentration of ice nucleating particles (INPs) and the ice crystal number concentration (ICNC) remains unresolved and limits our understanding of ice formation and hence precipitation amount, location and intensity. Enhanced ice formation through secondary ice production (SIP) could be accounting for this discrepancy. Here, we present the results from a sensitivity model study in the Eastern Swiss Alps with additional simulated in-cloud SIP

5 on precipitation formation and consequently on surface precipitation. The SIP processes considered include rime splintering, droplet shattering during freezing and breakup through ice-ice collisions. We simulated the passage of a cold front at Gotschnagrat, a peak at 2281 m above sea level (a.s.l.), on 7 March 2019 with COSMO, at a 1 km horizontal resolution, as part of the RACLETS field campaign in the Davos region in Switzerland. The largest simulated difference in the ICNC at the surface originated from the breakup simulations. Indeed, breakup caused a 1 to 3 order of magnitude increase in the ICNC compared

10 to SIP from rime splintering or without SIP processes in the control simulations. The ICNCs from the collisional breakup simulations at Gotschnagrat were in better agreement with the ICNCs measured on a gondola near the surface. However, these simulations were not able to reproduce the ice crystal habits near the surface. Enhanced ICNCs from collisional breakup reduced localized regions of higher precipitation and thereby improving the model performance in terms of surface precipitation over the domain.

1 Introduction

Clouds consisting only of liquid droplets contribute only a small fraction to the overall precipitation on earth (Heymsfield et al., 2020). Indeed, diffusional growth is slower for larger droplets, becoming inefficient for droplets larger than 20 µm in diameter when updraft velocities are weak (Wang, 2013). In the presence of stronger local updrafts, cloud droplets can also grow by collision-coalescence with other droplets to form raindrops. Simultaneously, the cloud droplets are transported to temperatures

20 colder than 0 °C where they are supercooled and can freeze heterogeneously, i.e. with the aid of an ice nucleating particle (INP).

The co-existence of ice crystals and supercooled liquid water droplets in clouds plays a significant role in the formation of precipitation in the mid-latitudes (Mülmenstädt et al., 2015). These clouds are known as mixed-phase clouds (MPCs) and can be found in the temperature regime between 0 to approximately -38 °C (Korolev and Mazin, 2003; Morrison et al., 2012;

25 Lohmann et al., 2016a). Once ice crystals exist in a supercooled liquid cloud, the cloud becomes thermodynamically unstable

and the ice crystals grow at the expense of the liquid water droplets. The liquid droplets may eventually evaporate completely in the vicinity of the growing ice crystals. This process is called the Wegener-Bergeron-Findeisen process (WBF: Wegener, 1911; Bergeron, 1965; Findeisen et al., 2015) and can lead to rapid partial or full glaciation of MPCs (Blyth and Latham, 1997), e.g. when updrafts are less than $1 \, \text{m s}^{-1}$ for an integral ice crystal radius of $100 \, \mu\text{m cm}^{-1}$ (Korolev, 2007). To sustain MPCs the

30 supersaturation with respect to water must be maintained to compete with the depletion of water vapor by depositional growth of ice particles (Korolev and Isaac, 2002; Bühl et al., 2016). In such environments, a continuous source of cloud droplets are supplied which can grow in the vicinity of ice crystals. For example, mountainous regions can provide a continuous source of liquid droplets through a constant air flow that is forced to ascend due to the topography. In the Arctic regions, MPCs can develop subcloud (the layer extending from the surface to the cloud base) circulation leading to cold pool formation and

35 updrafts driving new convective cells (Morrison et al., 2012; Lohmann et al., 2016a; Beck et al., 2018; Eirund et al., 2019a). Thus, the MPC lifetime is very sensitive to the updraft velocity (Korolev and Mazin, 2003; Lohmann et al., 2016a). Lohmann et al. (2016a) showed that high updraft velocities, induced by steep orography, can stabilize a MPC. In this case, adiabatic cooling rate caused supersaturation with respect to liquid water to exceed the diffusional growth rate allowing both cloud droplets and ice crystals to grow (Korolev, 2007).

40 Primary production of ice crystals at temperatures warmer than homogeneous nucleation occurs through heterogeneous nucleation. In theory, the number concentration of INPs equals the ice crystal number concentration (ICNC) when no secondary ice production (SIP) process or surface-based processes (e.g. hoar frost or blowing snow) are active. However, airborne observations show that the ICNC can be orders of magnitude larger than the INP concentration (Field et al., 2016, and references therein). Field campaigns conducted at Jungfraujoch, in the Bernese Alps in Switzerland, also showed that surface-based mea-

45 surements of ICNC exceed INPs by several orders of magnitude (Henneberger et al., 2013; Beck et al., 2018). A modelling study conducted by Henneberg et al. (2017) over the Bernese Alps showed that simulated ICNC during winter are underestimated by an order of magnitude in MPCs as compared to the observations taken by Lloyd et al. (2015). Temperatures were between -8 and -15 °C and therefore too cold to trigger existing SIP processes through rime splintering, also known as the Hallett-Mossop process (Hallett and Mossop, 1974). Rime splintering occurs at warmer temperatures, between -3 and -8 °C,

50 and dominates ice multiplication in the early stages of the cloud's existence. However, a cold cloud base leads to slower diffusional droplet growth. In this case, the cloud droplets remain smaller than the required 24 µm in diameter that is needed for multiplication through rime splintering (Hallett and Mossop, 1974). This cold cloud base could dampen the immense multiplicative nature of rime splintering revealing the dominance of other possible mechanisms for multiplication early in a cloud's existence, for example, the collisional breakup of ice particles (Yano and Phillips, 2010a). The collisional breakup

55 of ice particles is a result of the ice-ice collisions and was found to be most active at -15 °C. Vardiman (1978) showed that collisional breakup occurs when large concentrations of rimed ice crystals are present in convective clouds, which increases SIP significantly.

Numerical formulations have been developed to describe SIP by the collision of different ice species (e.g. Phillips et al., 2017), e.g. when graupel collides with ice crystals, when ice crystals collide with snow (e.g. Yano and Phillips, 2010a;

60 Sullivan et al., 2018a) or when larger graupel collides with smaller graupel (Sullivan et al., 2017, 2018b; Sotiropoulou et al.,

2020). Therefore, the mass concentrations of the collider species must be adequately simulated (e.g Otkin et al., 2006) as any misrepresentation in the graupel category could potentially lead to significant differences in the SIP rate. There are, however, only a small number of studies that have used these collisional breakup parameterizations in mesoscale models (e.g., Sullivan et al., 2018a; Hoarau et al., 2018; Sotiropoulou et al., 2020). Notably, Sullivan et al. (2018a) demonstrated that the lack of

65   graupel formation in a cold frontal rainband in modeling simulations compared to observations (Crosier et al., 2014) caused collisional breakup to be two orders of magnitude less effective in the SIP compared to rime splintering. Graupel was the only ice species that could cause collisional breakup when they collided with either ice crystals or snowflakes. Sullivan et al. (2018a) could, however, address the discrepancy between ICNC and INP concentrations in their simulations by using the rime splintering, collisional breakup, and droplet shattering processes simultaneously. In a modeling study, Sullivan et al. (2018b)

70   showed that a warm cloud base, between 20 and 25 °C, at an updraft velocity of $4\,\mathrm{m\,s^{-1}}$, is required for cloud droplets to grow large enough through coalescence or condensation to freeze and then shatter. As the cloud base temperature and updraft velocity decrease, droplet shattering becomes less efficient.

Several other mechanisms like hoar frost and blowing snow have been suggested as surface flux processes that could lift ice particles from the surface of mountains and increase the ICNC of winter orographic MPCs (Rogers and Vali, 1987; Farrington

75   et al., 2016; Beck et al., 2018). Farrington et al. (2016) simulated ICNC at Jungfraujoch with a simplified parameterization for hoar frost. However, this parameterization is independent of the surface concentrations of hoar frost which could alter the accuracy of the surface flux. ICNC enhancement due to hoar frost and blowing snow could also aid in enhancing further SIP processes, but currently, it is unknown which of these processes dominates under different conditions. Understanding and representing the ICNC through the cloud, and not only at the base of the cloud due to surface processes, can also aid in a

80   better representation of the surface shortwave budget (Young et al., 2019). Independent of surface processes, hoar frost and blowing snow, we are investigating the discrepancy between ICNC and INP concentrations from the perspective of SIP to examine two points. Firstly, how active SIP processes are in wintertime orographic MPCs, and whether they could explain the observed ICNC in a case study of the RACLETS (Role of Aerosols and CLouds Enhanced by Topography and Snow) field campaign. Secondly, what is the effect of SIP processes on the cloud microphysics in terms of precipitation formation, location

85   and intensity.

2   Methods

2.1   Case study of the RACLETS field campaign

The RACLETS campaign took place in February and March 2019 in the Davos region in Switzerland (also introduced in Ramelli et al. (2020); Lauber et al. (2020)). Its goal was to improve our understanding of the influence of both orography and

90   aerosols on the development of clouds and on precipitation formation. Of particular interest, a cold front passed over the Swiss Alpine region on 7 March 2019 and was captured by measurements of precipitation and in-situ measurements of cloud droplets, ice crystals and INPs. The precipitation rate data and the liquid water path (LWP) data were provided by the Leibniz Institute for Tropospheric Research (TROPOS). The precipitation rate was collected from rain gauge data when available. Otherwise,

the precipitation rate was estimated by an upward pointing radar situated at Davos Wolfgang, 1630 m a.s.l. at a temporal
95   resolution of 30 s. However, the radar attenuation from 8:15 to 14:00 UTC was not corrected for. As a result, no estimation of
supercooled liquid within the MPC could be made. The LWP was estimated by the microwave radiometer that was situated at
the same location as the radar. We also used the precipitation data from MeteoSwiss in the form of a CombiPrecip product,
which is computed using a geostatistical combination of radar estimates from plan position indicator radar data with rain-gauge
measurements (Sideris et al., 2014). We used CombiPrecip to capture the spatial extent of the precipitation over the Swiss Alps
100   at an hourly resolution.

Furthermore, ice crystal properties were collected using the HoloGondel platform installed on the Gotschnabahn (described
in Lauber et al., 2020), which consists of several instruments including the HOLographic Imager for Microscopic Objects
3G (HOLIMO 3G in Beck et al., 2017). The outcome product of HOLIMO 3G are 2D images of cloud particles, which
can be differentiated in ice and liquid particles for particles larger than 25 μm depending on the shape of the ice particles
105   (Henneberger et al., 2013). The separation between liquid droplets and ice crystals was done with a fine-tuned version of the
neural network described in Touloupas et al. (2020) with an overall uncertainty of the ICNC of ±10%. Above that, the ice
crystals were manually classified into irregular, pristine, rimed and aggregated particles, which provides valuable information
of the precipitation formation process in orographic MPCs. Note that ice crystals can also be rimed aggregates and thus fall
into two categories. Because of the total small number of recorded ice crystals and their different categories, the counting
110   uncertainty ($\sqrt{N}/V$; N: number of crystals, V: measurement volume) was added to the overall uncertainty for the ICNC as
well as for the different categories.

HoloGondel was installed on a cable car on the Gotschnabahn, which runs on the north-west side of the ridge towards
Gotschnagrat (2281 m a.s.l.), north of Davos Wolfgang (see Fig. 1 for the exact location). HoloGondel took in-situ images of
ice crystals and droplets within the cloud during 3 separate ascents of the Gotschnabahn running at the upper section between
115   Gotschnaboden (1790 m) and the Gotschnagrat mountain station (2280 m), specifically at 11:54, 12:54 and 13:26 UCT on 7
March 2019. During these times, temperatures ranged between -2.8 and 0.7 °C between Gotschnaboden and Gotschnagrat.

2.2 Model setup

2.2.1 Spatial and temporal resolution

For the purpose of better understanding precipitation formation, we used the non-hydrostatic limited-area atmospheric model
120   of the Consortium for Small Scale Modelling (COSMO; Baldauf et al., 2011) version 5.4.1b. COSMO has recently been used
to study wintertime orographic MPCs in the Swiss Alps (Lohmann et al., 2016a; Henneberg et al., 2017). The model domain
roughly covers a region of 500×400 km² (45.5 to 49.5° N and 6 to 13° E) at a horizontal resolution of 1 km (Fig. 1). For
reference, Davos Wolfgang is situated at 46.835° N and 9.85° E. A height based hybrid smoothed level vertical coordinate
system (Schär et al., 2002) with 80 levels was used and stretched from the surface to 22 km. The applied orographic smoothing
125   at a horizontal resolution of 1.1×1.1 km reduces the elevation of Gotschnagrat (located at 2 300 m a.s.l) to 1 880 m a.s.l.. For
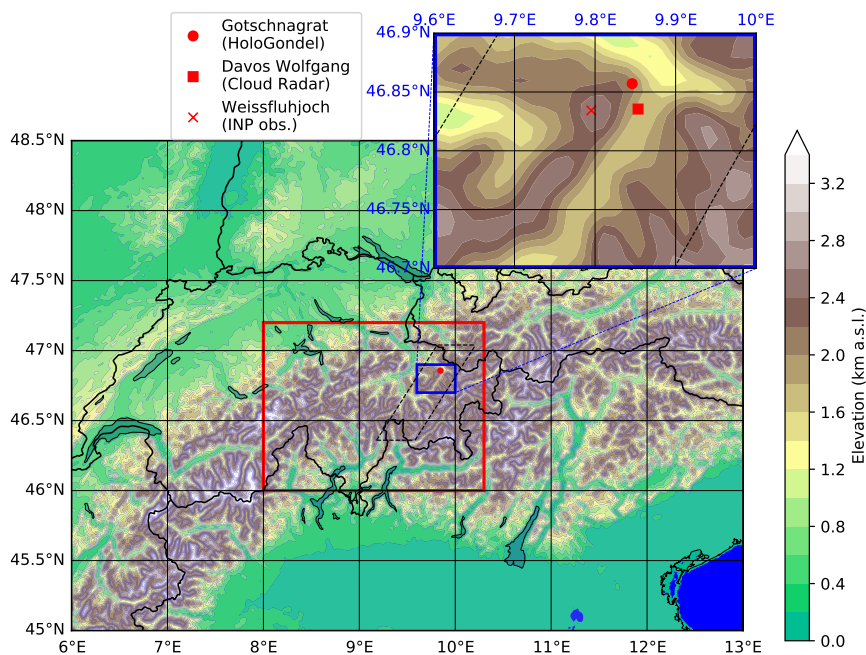
Figure 1. Overview of the model orography and the instrument location setup. The large domain is the simulated area that contains the analysis domain (red box). The enlarged blue domain is the locations where measurements were taken during the RACLETS campaign. The parallelogram (dashed black lines) is the domain of the flow-oriented vertical cross-section.

this study, we simulate the cold front passage between 9:30 and 14:45 UTC on March 7, 2019. Hourly initial and boundary conditions analysis data at a horizontal resolution of 7×7 km, supplied by MeteoSwiss, were used to force COSMO.

Simulations were conducted with the SIP processes, where several SIP processes were active at the same time and a control simulation (CNTL) where none of the SIP processes was active. For each of these simulations, 5 ensemble simulations are conducted by perturbing the initial temperature conditions at each grid point through the model domain with unbiased Gaussian noise at a zero mean and a standard deviation of 0.01 K (Selz and Craig, 2015; Keil et al., 2019).

2.2.2 Cloud microphysics scheme

We use a two-moment cloud microphysics scheme within COSMO with six hydrometeor categories, including hail, graupel, snow, ice crystals, raindrops and cloud droplets (Seifert and Beheng, 2006). INPs available for immersion freezing is prognostic throughout the simulations and are implemented following Possner et al. (2017) and Eirund et al. (2019b). The immersion freezing parameterization follows the DeMott et al. (2015) (D15) temperature dependence and reproduces the depletion and replenishment of INPs. The initial aerosol concentration for particles larger than 0.5 μm in diameter required for estimating the INP concentration was measured at Weissfluhjoch (2670 m a.s.l.) in clear air condition between 8:00 and 8:58 UTC on March 5, 2019. The average aerosol concentration larger than 0.5 μm during this time was $3.32\,\mathrm{cm}^{-3}$ at an ambient air temperature of

140 261 K (Seifert, 2019). For more accurate INP concentration estimates it is required that the ambient air temperature is colder than 258 K (DeMott et al., 2010) and, therefore, we also used the retrieved aerosol concentration from the upward-pointing LIDAR that was situated at Davos Wolfgang. The LIDAR retrieval gave a full vertical profile of the atmosphere. At temperatures between 258 and 243 K, the aerosol concentration larger than 0.5 µm was between 1.8 and 2.5 cm^{-3} for which we then accordingly chose 2 cm^{-3} as input for the D15 parameterization. At a temperature of 243 K, the estimated INP concentration

145 was 23 L^{-1}. The freezing of raindrops occur heterogeneously and independent of INPs. This is because the raindrop number concentration is at least 10^3 smaller than the CNDC and has an insignificant contribution to the primary production of ice crystals upon freezing (Figs. S4 and S5i and j). It is included in our simulations because without this parameterization droplet shattering can not occur. In the spectral partitioning of freezing rain, only the frozen raindrops that are partitioned as ice crystals (Blahak, 2008) can cause multiplication through droplet shattering as discussed in the following section.

150 **2.2.3 Secondary ice processes parameterizations**

Besides the primary ice formation pathways through homogeneous and heterogeneous nucleation of cloud droplets and raindrops, rime splintering is the only process included in the standard version of COSMO that can enhance the ICNC otherwise. The rime splintering process has been parameterized, implemented and tested in numerical weather models (Blyth and Latham, 1997; Ovtchinnikov and Kogan, 2000; Phillips et al., 2006; Milbrandt and Morrison, 2015; Phillips et al., 2017). In COSMO,

155 rime splintering occurs exclusively after collisions between supercooled cloud droplets of diameter greater than 25 µm or raindrops with ice crystals, snow, graupel or hail, all larger than 100 µm (e.g Phillips et al., 2006) at temperatures between -3 and -8 °C (Hallett and Mossop, 1974). The predominant theory is that within this temperature range the supercooled droplets that rime on large ice particle freeze resulting in a buildup of internal pressure whereby the pressure is relieved when the frozen shell cracks and produces secondary ice particles (Hallett and Mossop, 1974). At temperatures colder than -8 °C the ice shell of

160 the frozen droplet is too strong to break (Griggs and Choularton, 1983) and at warmer temperatures than -3 °C the supercooled droplet spread over the ice particle not causing any SIP (Dong and Hallett, 1989). However, SIP has also been observed at temperatures where the Hallett-Mossop droplet size and temperature requirements were not satisfied.

Droplet shattering produces maximum splinters at around -15 °C when large droplets freeze and shatter if the internal pressure build-up is high enough to eject fragments (e.g. Kolomeychuk et al., 1975; Leisner et al., 2014; Wildeman et al.,

165 2017; Lauber et al., 2018; Keinert et al., 2020). So far, other than the temperature at which maximum droplet shattering occurs, there is no temperature constraint on this process which can be specifically important at temperatures close to -15 °C (Korolev et al., 2020; Lauber et al., 2020). The pressure build-up occurs mainly due to the unique characteristic of liquid water having a higher density than ice and thus expanding when it freezes. Larger droplets are more likely to shatter and likely produce more ice splinters (Kolomeychuk et al., 1975; Lauber et al., 2018). However, as of yet the number of splinters that are produced

170 during droplet shattering could not be quantified. A more rigorous formulation for the fragment number remains a challenge due to the lack of measurement in laboratory studies. Lauber et al. (2018) showed the highest fragment rates occur at 258 K, however, this was only for droplet sizes of 83 and 310 µm. Droplet shattering is parameterized as the product of a fixed fragment number, a temperature-dependent shattering probability given by a normal distribution in temperature and the existing droplet

freezing tendency used by Seifert and Beheng (2006). The normal distribution is centered at 258 K with a standard deviation
175   of 5 K and a maximum probability of 10 % as illustrated in Fig. 2a).

The collisional breakup of ice particles, in ice-ice collisions, was introduced and studied in laboratory experiments by
Vardiman (1978) and Takahashi et al. (1995) and found to be most effective at -15 °C. Takahashi et al. (1995) enfored the
collision of large, 1.8 cm in diameter, heavily rimed ice particles with one another and generated secondary ice particles
of up to 10^3 per collision. Yano and Phillips (2010b) and Yano et al. (2016) have demonstrated the generation of massive
180   enhancement of the ICNC by SIP due to ice-ice collision in a dynamical system-type model. Recently, Phillips et al. (2017)
developed a more physically robust theoretical parameterization, that was also applied in numerical simulations that consider
energy-conservation. In our case, following Sullivan et al. (2018a), we take a more simplified approach. The collisional breakup
of ice particles in the laboratory work of Takahashi et al. (1995) resulted in a temperature-dependent parameterization of the
fragment number:

185   $$\aleph_{\mathrm{BR}} = \frac{F_{\mathrm{BR}}}{\alpha}(T-252)^{1.2}\exp\left[-(T-252)/\gamma_{\mathrm{BR}}\right],\tag{1}$$

$$\left.\frac{\partial N_{\mathrm{ice}}}{\partial t}\right|_{\mathrm{BR}} = -\aleph_{\mathrm{BR}}\left.\frac{\partial N_j}{\partial t}\right|_{\mathrm{coll},jk}\tag{2}$$

where α is the scale factor, F_{BR} is the fragments generated during each collision, T is the temperature in Kelvin and γ_{BR}
is the decay rate of fragment number at warmer temperatures. In our breakup simulations, F_{BR} and γ_{BR} are the experimental
190   factors that are adapted for evaluating the collisional breakup parameterization. The fragment number $\aleph_{\mathrm{BR}}$ is multiplied by the
collisional tendency $\partial N_j/\partial t$ of the colliding hydrometeor pairs to calculate the number of ice crystals generated per time step
$\partial N_{\mathrm{ice}}/\partial t$ in Eq. (2). As shown in Fig. 2b), no collisional breakup occurs for temperatures below 252 K. Takahashi et al. (1995)
forced the collision between heavily rimed ice particles at a velocity of $4\,\mathrm{m\,s^{-1}}$. However, when the collision speed from the
experiment is used to calculate the size of the involved graupel particles, a $4\,\mathrm{m\,s^{-1}}$ fall speed corresponds to graupel particles
195   in the range of 2.5 mm in diameter according to Lohmann et al. (2016b). Considering the size-mass and fall-mass relations
that are used in COSMO, Blahak (2008) showed that for graupel and hail falling at $4\,\mathrm{m\,s^{-1}}$ the effective diameters were 4 mm
and 1.4 mm respectively. Also, in the simulations conducted here, graupel sizes would very rarely exceed 3 mm in diameter
(not shown here). Therefore, having smaller graupel particles than what was used in Takahashi et al. (1995), we expect $\aleph_{\mathrm{BR}}$
to be less and thus we introduce α to prevent extreme overestimations in $\aleph_{\mathrm{BR}}$ (Table 1). Another consideration to take into
200   account is that COSMO treats snowflakes as unrimed particles and as soon as riming occurs on snowflakes, the snow mixing
ratio is converted to the graupel mixing ratio causing especially large graupel mixing ratio (Otkin et al., 2006). Since graupel
is the only contributor to SIP through collisional breakup, increased graupel mixing ratios could lead to excessive SIP. Further
sensitivity studies were conducted with γ_{BR} of 2.5 instead of 5 as described in the parameterization used by Sullivan et al.
(2018a). When γ_{BR} is 2.5, $\aleph_{\mathrm{BR}}$ will be reduced at warmer temperatures (Fig. 2b).

205   In the standard version of COSMO, the ICNC after each model time step is limited to $500\,\mathrm{L^{-1}}$ for each level. However,
measurements showed that the ICNC within MPCs produced higher ICNC of up to $1014\,\mathrm{L^{-1}}$ (Lohmann et al., 2016a). Korolev

Table 1. Sensitivity settings for the collisional breakup parameterization. α is the scale factor, F_{BR} the fragments generated and γ_{BR} the decay rate of fragment number at warmer temperatures. In bold is $\gamma_{BR} = 5$ as used in by Sullivan et al. (2018a).

α	F_{BR}	$\gamma_{\mathbf{BR}} = \mathbf{5}$	$\gamma_{BR} = 2.5$
4	70	**BR70_T**	BR70
10	28	**BR28_T**	BR28
20	14	**BR14_T**	BR14
100	2.8	**BR2.8_T**	BR2.8
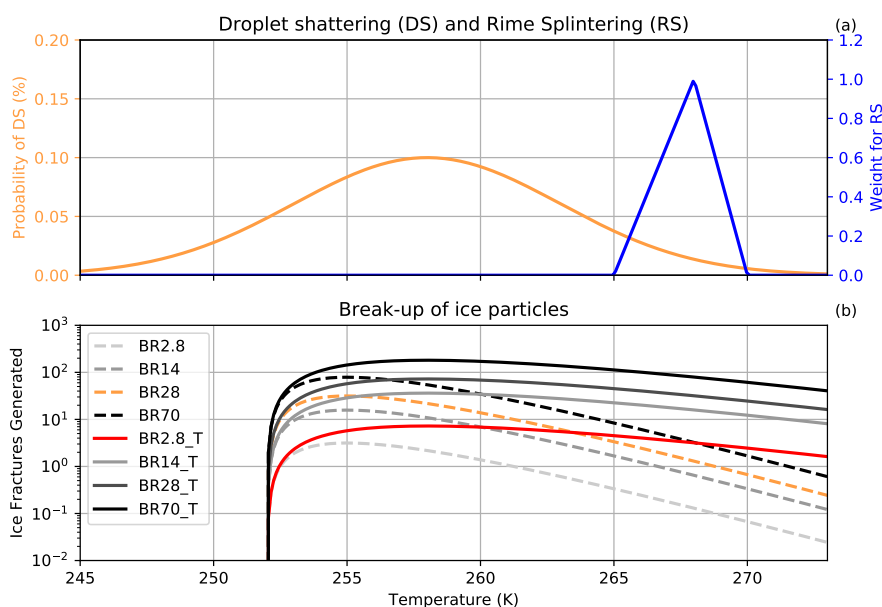
Figure 2. Secondary ice production processes at their defined temperature ranges. In a) is the probability of occurrence of droplet shattering (DS) and the triangular weighting function of HM. In b) is the fragment numbers generated by ice-ice collisional breakup (BR) for the different cases shown in Table 1. The red and yellow lines in b) are the collisional breakup parameterizations that were analyzed in the results.

et al. (2020) identified midlatitude frontal cloud systems within a temperature range of -15 and $0\,^\circ\text{C}$ to have 500 to $1000\,\text{L}^{-1}$ small faceted ice crystals. Therefore, we increased the ICNC limit to $2000\,\text{L}^{-1}$ in our model setup.

210 Using droplet shattering as the only active SIP process in our case study yields very similar results to the CNTL simulations with the exception that the SIP rate between 4 and $5\,\text{km}$ was $0.01\,\text{L}^{-1}\,\text{s}^{-1}$. Therefore, it was not included in the rest of our analysis (Fig. S1). Also, the initial analysis of the simulations with collisional breakup (for $\gamma_{BR} = 2.5$) showed that the SIP rate is between 1×10^{-3} and $7\,\text{L}^{-1}\text{s}^{-1}$ below $5\,\text{km}$ yielding an ICNC between 0.1 and $300\,\text{L}^{-1}$ at the surface (Fig. S2a, g). Contrasted

against these simulations are the collisional breakup simulations (for $\gamma_{BR} = 5$) that showed an increased SIP rate between 100 to $1000\,\mathrm{L^{-1}\,s^{-1}}$ yielding ICNC of $2000\,\mathrm{L^{-1}}$ at the surface at Gotschnagrat (Fig. S3a, g). These ICNCs were strongly influenced

215 by the ICNCs extending from the surface to 5 km. We chose the BR2.8_T settings because the ICNC was represented best near the surface at Gotschnagrat and that the ICNC hard limit did not impact the simulations and therefore collisional breakup and its impacts on the MPC can be understood better. Further, we used the BR28 simulation as a comparison to understand what the effect would be by reducing the SIP at warmer temperatures than 263.5 K while at the same time increasing the SIP at colder temperatures than 263.5 K compared to the BR2.8_T settings (Fig. 2b). Higher ice particles number concentrations at colder

220 temperatures can increase the competition for available cloud liquid water and glaciate the clouds at a faster rate slowing down precipitation formation. Due to their smaller size as a result of the aggressive collisional breakup, these ice particles should have slower sedimentation velocities. We do expect that precipitation formation will be slower in the BR28 simulations and that there will be a leeward shift in surface precipitation assuming that the lower part of the MPC is supersaturated with respect to water.

3 Results

225

3.1 Modeling ICNC and ice crystals growth rates at Gotschnagrat

3.1.1 Modeling ICNC

During each ~2 min ascent, the HoloGondel platform on the cable car recorded ice crystal concentrations averaged over three altitudes (1808-1961, 1961-2113 and 2113-2266 m). We first show the ICNC inferred from HoloGondel measurements on each

230 of its three ascents (at 11:54, 12:54 and 13:26 UTC) and as the outcome of COSMO simulations at Gotschnagrat (Fig. 1a). The holographic images yield size and habit information of the ice particles. From this information, the precipitation forming processes can be inferred (Fig. 3a, b). Note that the classification process for irregular ice particles is difficult to assign accurately as it can include aggregates of ice particles, blowing snow, ice particles sedimenting through different growth regimes or collisional breakup of ice particles. Therefore, the irregularly shaped particles can't be assigned to a specific category (e.g.

235 SIP). The total ICNCs from the observations were averaged over altitude for each ascent and were 16 ± 5, 19 ± 4 and $9\pm3\,\mathrm{L^{-1}}$ at 11:54, 12:54 and 13:26 UTC respectively. The simulated ICNC from the CNTL and rime splintering simulations was less than $0.1\,\mathrm{L^{-1}}$ below 2.15 km for both 12:00 and 13:00 UTC (Figs. 4 and 5a) and were at least 2 orders of magnitude smaller than the observations at Gotschnagrat (Fig. 3). Between 2.2 and 3.2 km, the SIP rate from rime splintering reached $5\times10^{-3}\,\mathrm{L^{-1}s^{-1}}$ (Figs. 4 and 5g). Rime splintering originated exclusively from raindrops, with diameters between 150 and 250 μm at a con-

240 centration of $0.1\,\mathrm{L^{-1}}$ that rimed onto ice particles (Fig. S4e, o). A diameter of 25 μm required for rime splintering to be active was not met by the cloud droplets, which only reached diameters of 20 μm (Fig. 4 and 5f). The CNTL and rime splintering simulations reached cloud droplet number concentrations (CDNCs) of $100\,\mathrm{cm^{-3}}$ and droplet diameters between 10 and 22 μm, aiding in the primary ice production. The low ICNC by the CNTL and rime splintering simulations emphasized the need to explore SIP with collisional breakup. The ICNC in the BR28 simulation was between 1 and $2\,\mathrm{L^{-1}}$ at 12:00 and 13:00 UTC

245 (Figs. 4 and 5a), within an order of magnitude of the HoloGondel observations. The ICNC from the BR2.8_T was higher between 10 and 12 L^{-1} which compared better to the HoloGondel observations, albeit with a high uncertainty below 3 km at 12:00 UTC. The SIP rate of collisional breakup was 2 orders of magnitude larger than rime splintering for 265 K≤T≤270 K. The ICNC from collisional breakup was significantly larger than the CNTL simulation above 3 km. This process resulted in lower liquid water and rain mass mixing ratios preventing primary ice production because of the absence of liquid water (Figs.

250 4 and 5a, b, c, g).

3.1.2 Modeling ice crystal growth rates

The enhanced SIP through collisional breakup had a significant impact on mostly glaciating the cloud above 2.5 km and can be seen in the nearly non-existent primary ice production rates due to the lack of cloud droplets (Fig. 4b, c). This also meant that the growth of ice crystals was mostly through vapor deposition that, in turn, suggests that the ice crystals were mostly

255 pristine above 2.5 km (Fig. 4d, h). Below 2.5 km a very shallow liquid layer, that was subsaturated with respect to water was present, causing ice particles to grow through the WBF process and/or riming at 12:00 and 13:00 UTC (Figs. 4, 5a, b, d, f) and S4d, e). The shallow mixed-phase cloud layer was of interest, because close to the surface the HoloGondel observations showed that rimed particles were dominant, making up 47 - 72 % of the total ICNC, indicating that the cloud (at least close to the surface), from 11:54 to 13:26 UTC, was in a mixed-phase state while passing over Gotschnagrat (Fig. 3b). Interestingly,

260 observed irregularly shaped ice crystals were also present that could have been artifacts from collisional breakup of ice or snow. However, it is also possible that the irregular ice crystals could have either been from ice crystals that fell through different growth regimes or they were from blowing snow. This would mean that only a subsection of the irregular ice crystals could have been from collisional breakup. Considering the lowest 700 m in the model we calculated the growth fraction of each of the growth mechanisms (riming, deposition and aggregation) of ice crystals (e.g. riming(%) = riming/(riming + deposition

265 + aggregation) from Table 2). This was done to compare the ice crystal classification to the HoloGondel observations. This was not meant to be a direct comparison because the ice crystals in the model could be rimed while also growing further by deposition and vice versa that could lead to double counting of processes. However, following this approach the BR2.8_T simulation showed that 2.6, 80.5 and 16.9 % of the growth was by riming, deposition and aggregation respectively at 12:00 UTC compared to the BR28 simulation showed growth fractions of 0.2, 80.3 and 19.5 %. At 13:00and 13:30 UTC the collisional

270 breakup simulations had growth by riming fractions of below 5.4 % suggesting that most of the ice crystals would have been either pristine or aggregated whereas the ice crystals observations were predominantly rimed in the observations. Evidently, the cloud liquid water that acts as rimers is underestimated in the collisional breakup simulations. These comparisons could not be carried over to the CNTL and rime splintering simulations due to the underestimated ICNC. The ice crystals that formed through primary ice production above 3 km sedimented through the overestimated liquid layer (Fig. 6b) and grew by deposition

275 and riming (acting as a stronger sink to the ICNC) resulting in higher conversion rates from ice crystals to graupel (Figs. 4 and 5b, c, d, h).
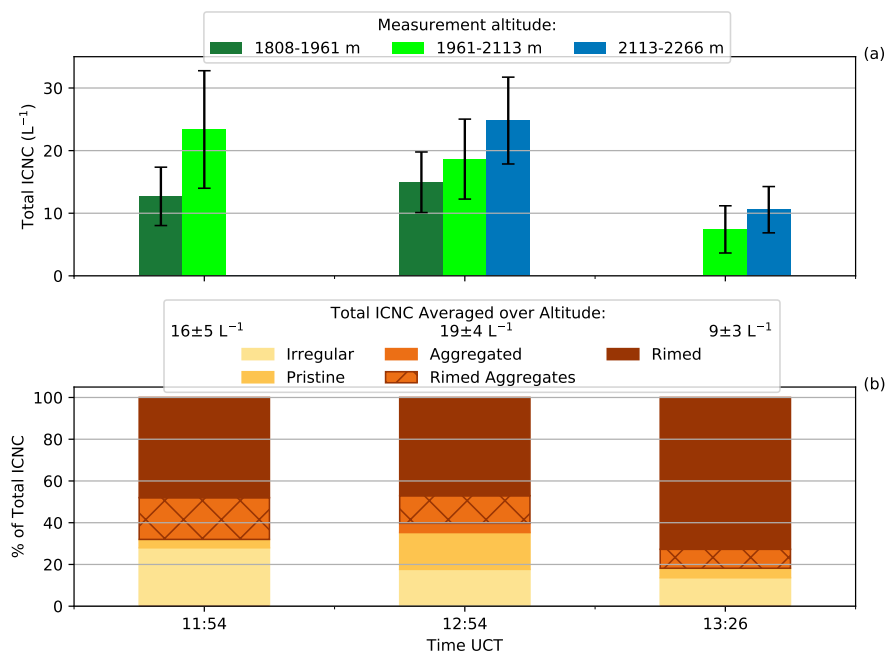
Figure 3. HoloGondel measurements on 7 March 2019. a) Total ICNC and measurement uncertainty (black error bars) of each Gondola run at each altitude. No measurements were taken at 11:54 UTC between 2113-2266 m and at 13:26 UTC between 1808-1961 m. b) Irregular, pristine, aggregated, rimed and rimed aggregate ice particles as the percentage of total ICNC averaged over the altitudes of each Gondola run.

Table 2. Vertically integrated growth rates ($mg\,m^{-2}s^{-1}$) of ice crystals over the lowest 700 m at Gotschnagrat. In brackets are the corresponding growth rate percentages.

		Gotschnagrat		
Simulation	Time (UTC)	Riming	Deposition	Aggregation
BR28	12:00	0.17 (0.2)	52.55 (80.3)	12.72 (19.5)
BR2.8_T		0.87 (2.6)	26.44 (80.5)	5.56 (16.9)
BR28	13:00	4.35 (5.4)	47.11 (59.0)	28.38 (35.6)
BR2.8_T		8.56 (2.6)	154.87 (47.7)	161.67 (49.7)
BR28	13:30	0.43 (0.1)	90.36 (24.8)	273.96 (75.1)
BR2.8_T		0.69 (0.1)	394.12 (52.9)	349.99 (47.0)

3.2 Modeling precipitation

To analyze the impact of ICNC on precipitation, we compared the cloud radar precipitation rate and the LWP from the microwave radiometer with that of the simulated precipitation rate and LWP. The observed precipitation started at 8:30 UTC
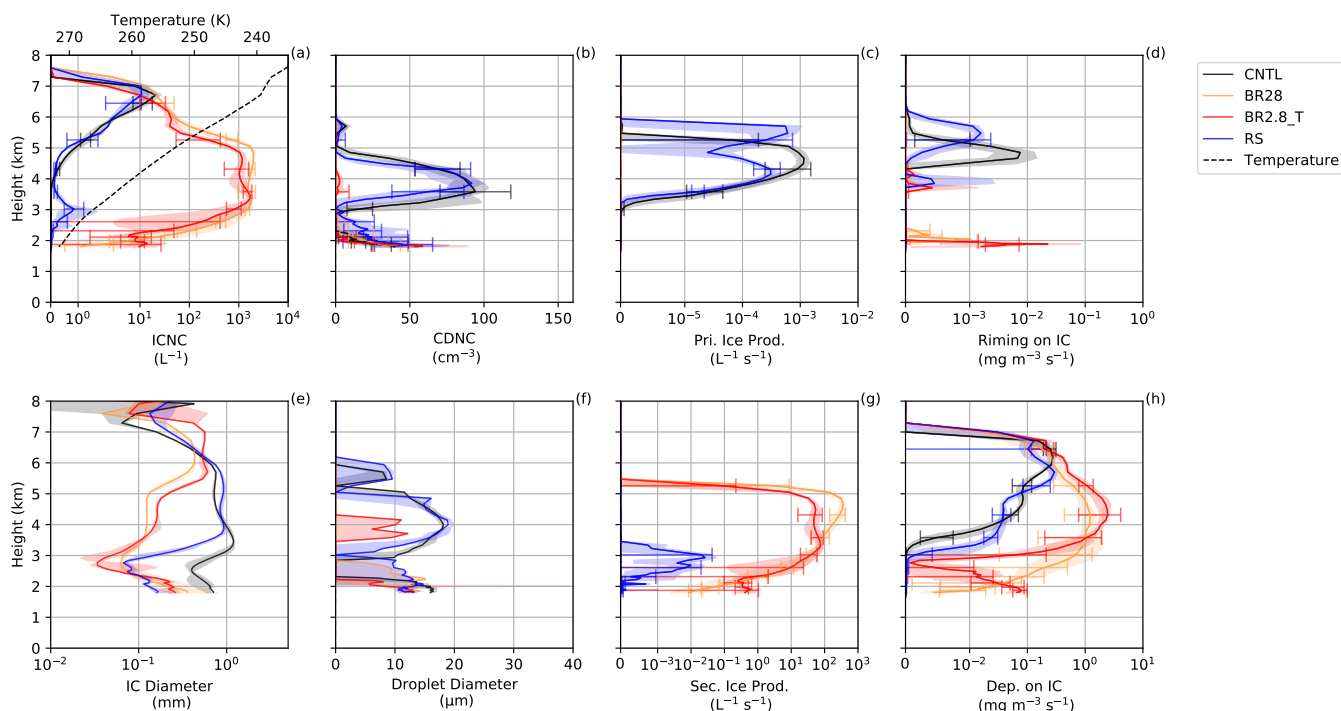
Figure 4. a) and e) Ice crystal number concentration (ICNC) and diameter, b) and f) cloud droplet number concentration (CDND) and diameter, c) and g) primary and secondary ice production, d) and h) riming and depositional (Dep.) growth of ice crystals at Gotschnagrat at 12:00 UTC. The solid lines are the model mean with error bars showing model spread for each simulation. The shaded regions are the minimum and maximum values for the four closest model points. Ice crystals are denoted by IC.

and continued until 14:00 UTC reaching maximum precipitation rates over 15 min intervals of 3.75 mm h^{-1} at 12:00 UTC as the cold front passed over Davos Wolfgang. All the simulations were unable to time the onset of the precipitation and underestimated the precipitation before 10:45 UTC (Fig. 6a). After 10:45 UTC the collisional breakup simulations overestimated the precipitation as compared to observations. The CNTL simulation also outperformed the rime splintering simulation which represented the precipitation rate more accurately. This underlines the difficulty that models have in simulating mountainous weather in general (Rotach and Zardi, 2007; Panosetti et al., 2018). The collisional breakup simulations, from 11:30 to 13:30 UTC, mostly underestimated the microwave radiometer liquid water path which resulted in the MPC consisting of less than 10 % liquid water (Fig. 6b, c).

As MPCs approach glaciation, precipitation formation through the WBF process slows down when the updraft velocity is not high enough to stabilize the MPC (Korolev and Mazin, 2003). In the collisional breakup simulations, in which the ICNCs were between 10^1 and 10^3 L^{-1}, the updraft velocities were on the order of -0.2 to 0.6 m s^{-1} at altitudes between 1.7 and 4.3 km. A liquid layer (cloud liquid water larger than 0.1 mg m^{-3}) was present at the surface that extended to approximately 1.6 km
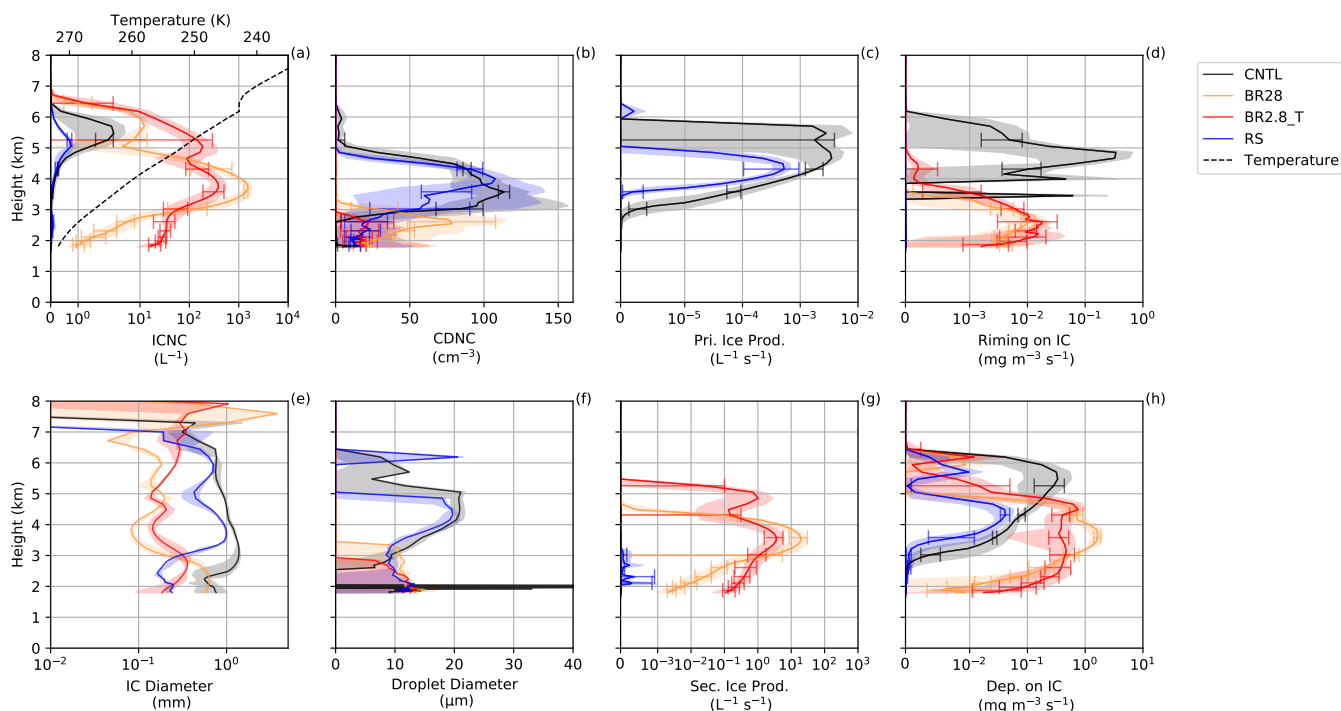
Figure 5. a) and e) Ice crystal number concentration (ICNC) and diameter, b) and f) cloud droplet number concentration (CDND) and size, c) and g) primary and secondary ice production, d) and h) riming and depositional (Dep.) growth of ice crystals at Gotschnagrat at 13:00 UTC. The solid lines are the model mean with error bars showing model spread for each simulation. The shaded regions are the minimum and maximum values for the four closest model points. Ice crystals are denoted by IC.

above the surface from 12:00 to 13:00 UTC. Most of this layer, however, was subsaturated with respect to water and the ice particle growth was via the WBF process aided in precipitation formation.

In Fig. 7 we consider the precipitation over the larger domain (e.g. the red box in Fig. 1). The average wind direction
295 between 12:00 and 14:00 UTC, and between 2 to 4 km above the surface, came from the south-west (indicated by the red arrow on Fig. 7a). In general, the spatial precipitation patterns of all the simulations over the domain have a moderate to strong relationship, correlations above 0.68 with high confidence, with CombiPrecip (Table. 3). Important here is that the Pearson correlation, in general, is sensitive to outliers in a skewed distribution which can lead to being a less desirable statistic. This was the case with surface precipitation over a domain and, therefore, we also calculated the interquartile ranges with the 25th
300 and 75th percentiles to compare the observations with the simulations. CombiPrecip had a narrower precipitation distribution indicated by the interquartile range between the 25th and 75th percentiles of $1.09\,\mathrm{mm\,h^{-1}}$ than all the simulations meaning that the precipitation had less variability. This can be seen in the domain as all the simulations had regions of localized high precipitation rates. This resulted in a higher variability with an interquartile range between 1.46 and $1.79\,\mathrm{mm\,h^{-1}}$ of which 75 % of the precipitation were between 1.7 and $2.14\,\mathrm{mm\,h^{-1}}$ (Fig. 8). Higher variability, e.g. in the CNTL and rime splintering
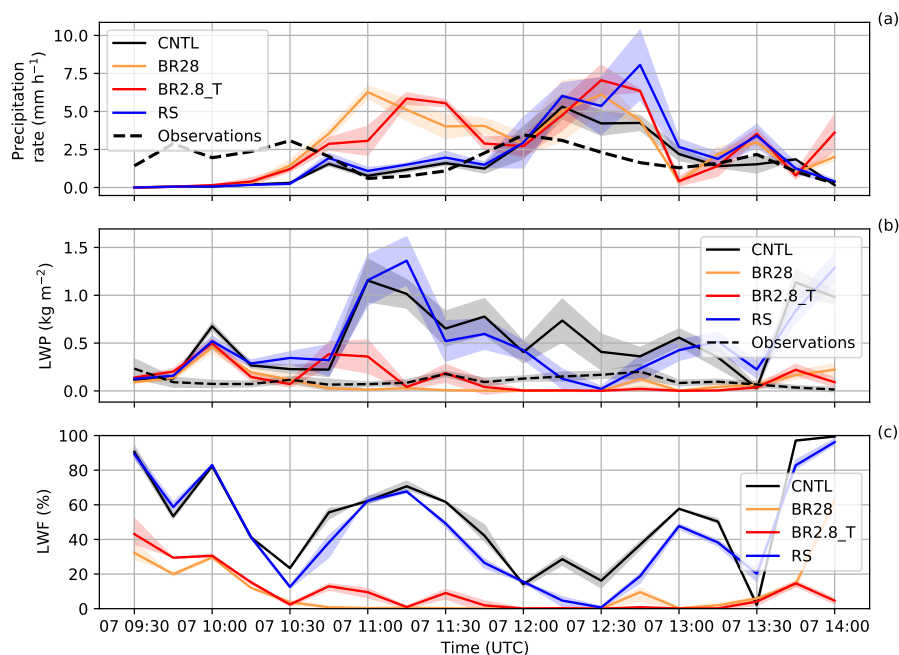
Figure 6. Time series of the a) Precipitation rate from the rain gauge and cloud radar and b) LWP from the microwave radiometer are compared to all the sensitivity simulations at Davos Wolfgang. We interpolated from the four closest model grid points to Davos Wolfgang. The shaded areas show the model spread for each simulation. c) is the LWF (%) from 9:30 to 14:00 UTC.

305   simulations, questions the better correlations. The localized regions of stronger convection and invigorated precipitation when the SIP processes were excluded, causing the higher variability, can most likely be attributed to the dynamics, rather than the cloud microphysics scheme. Craig and Dörnbrack (2008) demonstrated that a model resolution of ~1 km is approximately equal to the characteristic turbulence scales of convective structures. Therefore, using a 1D turbulence scheme, which we used and is generally used in cloud-resolving models, is not optimal and in the "grey zone". Also, horizontally homogeneous

310   conditions are assumed in most turbulence schemes and have been validated over flat terrain (e.g. Mellor and Yamada, 1982; Rotach and Zardi, 2007) which is not the case for our study. Earlier and higher precipitation rates can occur if mountains are high enough to force the flow into an elevated mixed layer leading to a faster transition of deep convection (Panosetti et al., 2018).

The localized regions of invigorated precipitation rates were suppressed by including the SIP processes. Because collisional

315   breakup is a mechanical process it doesn't contribute directly to the latent heat budget and, therefore, shouldn't invigorate the updraft velocities. However, larger number concentrations of ice particles can cause increased depositional growth and thereby change the buoyancy structure of the cloud. Stronger updrafts could then loft the smaller ice particles to higher altitudes reducing their sedimentation velocities towards the surface. Evidence for the effect of the strong SIP rate on ice particle size can be seen in Figs. S4 and S5k, l and m. The BR28 simulation, which was able to produce the largest SIP rates, resembled the

320   magnitude of the precipitation CombiPrecip the best by reducing more of the localized high precipitation regions of the CNTL simulation (e.g Fig. 9). To the north of Gotschnagrad, the cloud was mostly glaciated slowing precipitation down (Fig. 7c, f, i). Over the domain the spread of the precipitation between the 25th and 75th percentiles was $1.46\,\mathrm{mm\,h^{-1}}$ with 75 % of the precipitation below $1.79\,\mathrm{mm\,h^{-1}}$ (Fig. 7 c, d) and Table 3). Another interesting feature is that the rime splintering simulation caused a southward shift in the precipitation when compared to the CNTL simulation (Figs. 7b, h) and 11g). Not as obvious,

325   but similar in that the BR2.8 precipitation intensity lags behind that of the BR2.8_T simulations over the flow-oriented vertical cross-section in Fig. 11g). The faster precipitation formation is coupled to the higher ICNC within a MPC that can enhance riming as long as liquid droplets are present or else by the WBF process.

3.3   SIP impact on precipitation over the flow-oriented cross-section

The flow-oriented vertical cross-section as depicted in Fig. 7 helps to explain the behavior of the MPC with respect to enhanced

330   SIP (Fig. 10). The MPC cloud was defined by cloud droplet and ice crystal mixing ratios greater than 10 and $0.1\,\mathrm{mg\,m^{-3}}$ respectively. In the CNTL and rime splintering simulations, the mixed-phase part of the cloud extended to approximately 5 to 6 km and had a cloud top at 234 to 235 K. The rime splintering rate below 4 km was confined to $0.1\,\mathrm{L^{-1}s^{-1}}$ with the highest primary ice production rate of 0.01 to $0.1\,\mathrm{L^{-1}s^{-1}}$ between 4 and 7 km. The structure of the MPC did not change significantly due to the enhanced SIP. The additional ice crystal formation near the surface in the vicinity of the abundant cloud liquid

335   water caused a significant increase in the averaged depositional growth rates over the cross-section from 1.72 to $2.20\,\mathrm{g\,m^{-2}}$ (an increase by 28 %) while the riming rates also showed a small increase (Figs. 10d and 11e, f). Higher mass mixing ratios in snow and graupel, also reflected in the higher ice water fraction, were produced as a result of the faster conversion from ice crystals (Fig. 11a, c). This led to earlier and increased surface precipitation upstream of the flow direction over that of the CNTL simulation (Fig. 11g).

340   Collisional breakup had a distinct effect on the MPC reducing its vertical extent to around 4 km (Fig. 10b, d). In both of the collisional breakup simulations, the SIP reached $100\,\mathrm{L^{-1}s^{-1}}$ below 5 km impacting the primary ice production rate strongly due to the significant reduction in the LWP (Figs. 10b and 11d). As a result, there was a clear shift towards the depositional growth of ice particles from $46.4°$ N northwards. Korolev and Mazin (2003) showed that for high values of $N_i\bar{r}_i$ and updraft velocities between 0.1 and $1\,\mathrm{m\,s^{-1}}$ the ice particles will absorb water vapor rapidly reducing it to saturation over ice and therefore

345   controlling the supersaturation. Stronger combined growth rates of up to 33 % compared to the CNTL increased the latent heat release, updraft velocities and ultimately precipitation over the cross-section between 46.5 and $46.8°$ N. The BR2.8_T simulation, especially, overestimated the precipitation because of the higher SIP rates at warmer temperatures in the vicinity of cloud liquid water (Figs. 10c and 11g). North of $46.7°$ N the IWF was well above 95 % glaciating large parts of the MPC. Because of the loss of cloud liquid, precipitation formation was slowed down reducing the surface precipitation windward of

350   Gotschnagrat (Fig. 11c to g). This resulted in a mean precipitation rate over the cross-section that was $2\,\mathrm{mm\,h^{-1}}$ compared to CombiPrecip at $1.69\,\mathrm{mm\,h^{-1}}$. We also calculated the Pearson correlation between the sensitivity simulations and CombiPrecip in Fig. 11g. However, the BR2.8_T simulation correlation was the weakest at 0.19 while the CNTL, BR28 and rime splintering simulations correlated much better with CombiPrecip at 0.83, 0.59 and 0.69 respectively. The precipitation magnitude in
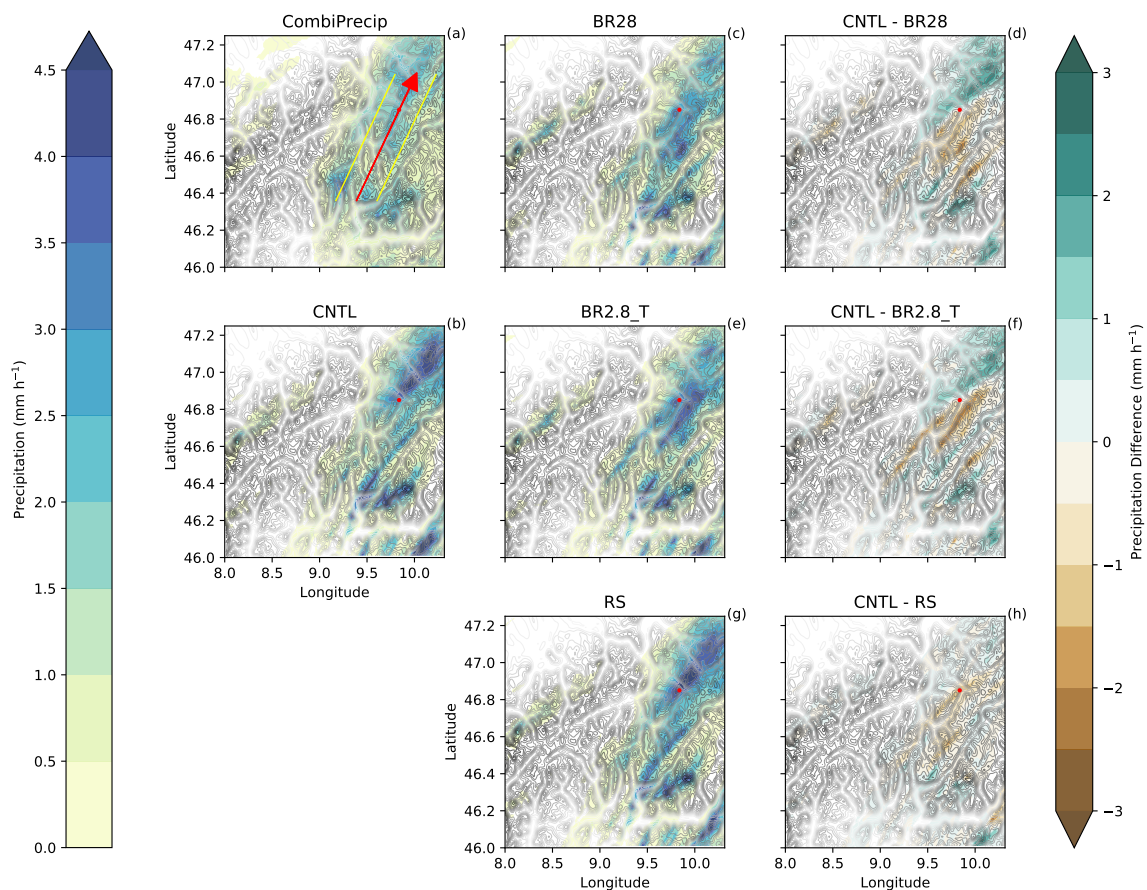
Figure 7. Precipitation rate (mm h^{-1}) over the domain. a) CombiPrecip, b) CNTL, c) BR28, d) CNTL - BR28, e) BR2.8_T, f) CNTL - BR2.8_T, g) RS and h) CNTL - RS between 12:00 and 14:00 UTC. The yellow lines are the outer limits of the cross-sections around the red arrow showing the wind direction. The red marker shows the location of Gotschnagrat and the grey shading is the topography between 0 (white) and 3700 m (dark grey).

the BR28 simulations matched the observed one better but was shifted towards the south which negatively influenced the correlation. In summary, we have shown that COSMO benefits from the inclusion of collisional breakup processes in simulating ICNC and precipitation.

4 Discussion

Our study suggests that including SIP through collisional breakup can enhance the in-situ ICNC and consequently surface precipitation. The collisional breakup simulations led to ICNCs at Gotschnagrat of one to two orders magnitude larger than in the rime splintering simulations. More precisely, the numbers were between 1 and 2 L^{-1} and 10 and 12 L^{-1} for BR28 and

Table 3. The interquartile range (IQR) between the 25th and 75th percentiles and median in mm h^{-1} for CombiPrecip and the sensitivity simulations. The Pearson correlation coefficient between CombiPrecip and the sensitivity simulations.

	IQR	25th perc.	75th perc.	Median	Pearson Corr.
CombiPrecip	1.09	0.41	1.50	0.93	
CNTL	1.60	0.35	1.94	1.60	0.73
BR28	1.46	0.33	1.79	1.46	0.68
BR2.8_T	1.51	0.32	1.83	1.51	0.70
RS	1.79	0.35	2.14	1.79	0.75
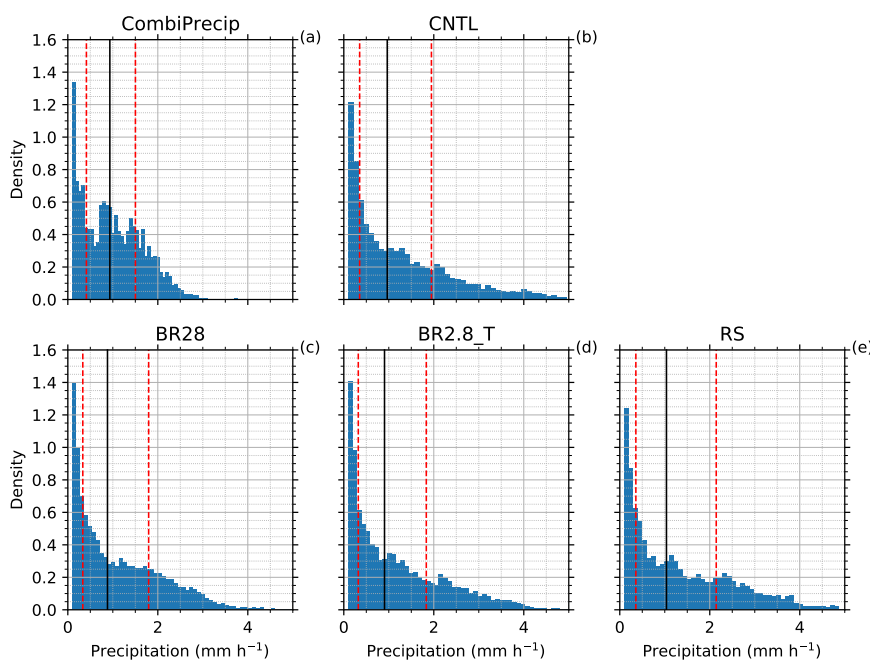
Figure 8. Precipitation rate (mm h^{-1}) histogram for a) CombiPrecip, b) CNTL, c) BR28, d) BR2.8_T and e) RS from the domains in Fig. 7. The median (black solid line) and the 25th and 75th percentiles (red dashed line).

BR2.8_T, respectively, compared to the rime splintering simulations of less than $0.1 \, \text{L}^{-1}$. The BR28 simulation most closely represented observations, albeit leading to ICNC an order of magnitude smaller than observed at Gotschnagrat. However, blowing snow cannot be excluded as a contributor to the measured ICNC (e.g. Farrington et al., 2016; Beck et al., 2018) even though we were not able to quantify this process in our analysis. As a consequence, the current discrepancy in ICNC between the BR28 simulation and the observations could be overestimated.

Surprisingly, our SIP rate through collisional breakup was between 10^4 to 10^6 times larger than what Sullivan et al. (2018a) reported in their cold front rainband study. We hypothesize that this large difference is due to the availability of cloud liquid

365
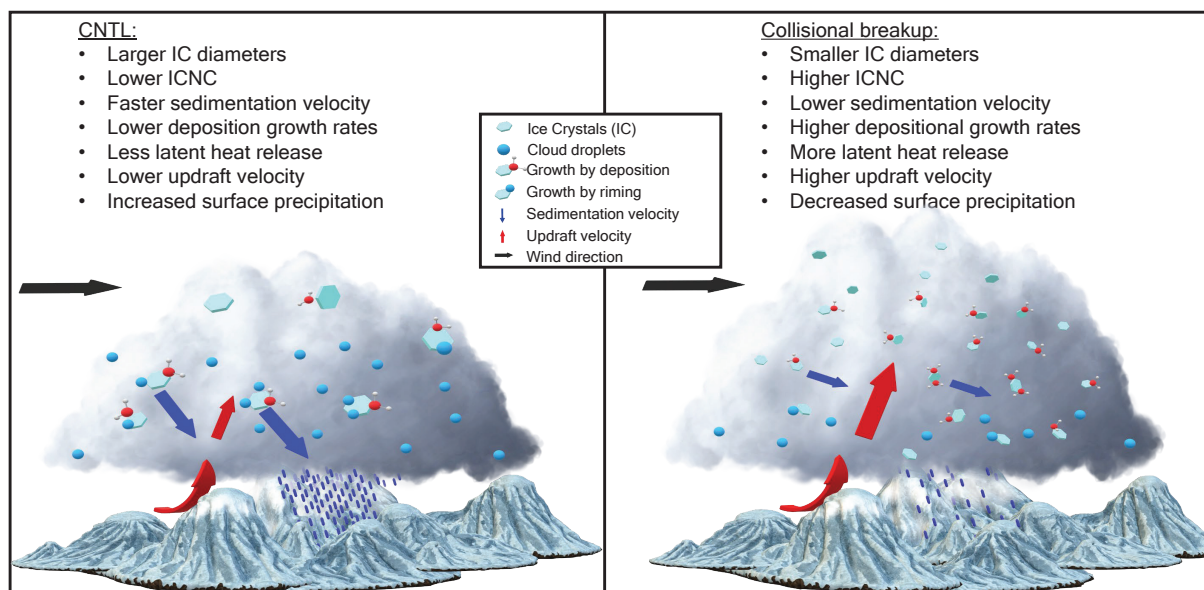
Figure 9. Schematic summary of the impact of collisional breakup of ice particles on the cloud structure and surface precipitation.

water that rimes onto ice crystals and snowflakes. This process converts ice and, especially, snow quickly to large quantities of graupel which causes higher SIP rates through collisional breakup. In the Sullivan et al. (2018a) case, graupel was noticeably

370   low, which limited graupel-ice/snow interactions. The low graupel concentrations meant that the SIP from collisional breakup simulation was at least 10^3 times smaller than that of the rime splintering simulation which was at around 10 to 100 L^{-1}. The excessive SIP rate through collisional breakup in our simulations, in combination with a larger graupel mixing ratio (Fig. 11a), is likely due to ideal conditions for collisional breakup (Fig. 9 Sullivan et al., 2018b). Indeed, our simulations have a cloud base temperature of around 273 K and averaged updraft velocities through our cross-section of up to $0.6\,\mathrm{m\,s^{-1}}$. The

375   large SIP rates, in our case, countered the stronger precipitation in localized regions. This decreased precipitation is in direct contrast to Sullivan et al. (2018a) showing that when using secondary ice parameterizations, regions of invigorated precipitation became even wetter. A possible explanation for the decreased precipitation is that the smaller ice particles in our collisional breakup simulations are lofted to higher regions within the cloud which is already glaciated in winter orographic MPC. These ice particles take a longer time to sediment to the surface and alter the location and intensity of the surface precipitation.

380   If the middle to the upper part of the cloud were not glaciated, we would have indeed, similar to Sullivan et al. (2018a), expected localized increase in surface precipitation due to faster ice particle growth. The SIP rates in our simulations compared better with Phillips et al. (2017) even though they simulated a convective storm with updrafts exceeding $5\,\mathrm{m\,s^{-1}}$ which is not comparable to the meteorological situation we simulated. However, in their case, the collisional breakup parameterization was more physically robust by including the kinetic energy of two particles, the fragility coefficients, humidity- and temperature-

385   dependent collision types into account.
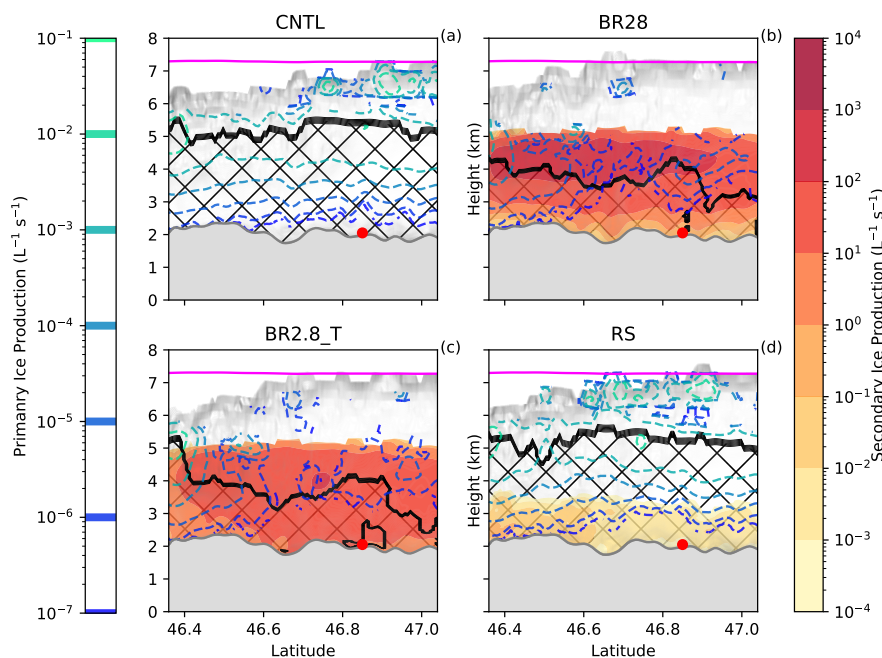
Figure 10. Secondary ice production and primary ice production (L^{-1} s^{-1}) averaged between 12:00 and 14:00 UTC for a) CNTL, b) BR28, c) BR2.8_T and d) RS. The hatched area is defined as the MPC where the cloud droplet mass concentration and ice crystal mass concentration is greater than 10 and 0.1 mg m^{-3} respectively. The pink line is the homogeneous freezing line at 235 K and the shaded grey area is the cloud area fraction.

As stated in 2.2.3, we set an ICNC threshold of 2000 L-1 in our model. This threshold strongly restricts the ICNC. Therefore, the full effect of using higher coefficients for F_{BR} could not be realized. We ran simulations with no ICNC threshold and observed evidence for violations against mass conservation in the model. This ICNC threshold is necessary, particularly in the collisional breakup simulations.

390   Another aspect that could enhance collisional breakup is the conversion from snow to graupel. For collisional breakup to occur, graupel formation is necessary. Graupel formation can only happen when either cloud droplets or raindrops rime onto ice crystals or snow. Because snow in the model is described as pristine (unrimed), a tuning parameter is used to rapidly convert snow to graupel when raindrops rime onto snow (Seifert and Beheng, 2006). Alongside this tuning parameter, Seifert and Beheng (2006) set a threshold to convert ice crystals and snow to graupel only if they are larger than 500 μm in diameter

395   to suppress the early formation of very small, 200 to 400 μm, graupel. As soon as graupel forms within the collisional breakup regime (temperatures warmer than 252 K), collisional breakup occurs. In the standard model version, the threshold has been set to 200 μm (e.g. Seifert and Beheng (2006)) which encourages earlier graupel formation. Using this threshold in conjunction with collisional breakup could be the a reason why we saw such large SIP rates. It is worthwhile to consider the size conversion threshold when secondary ice processes are used in cloud microphysics schemes.
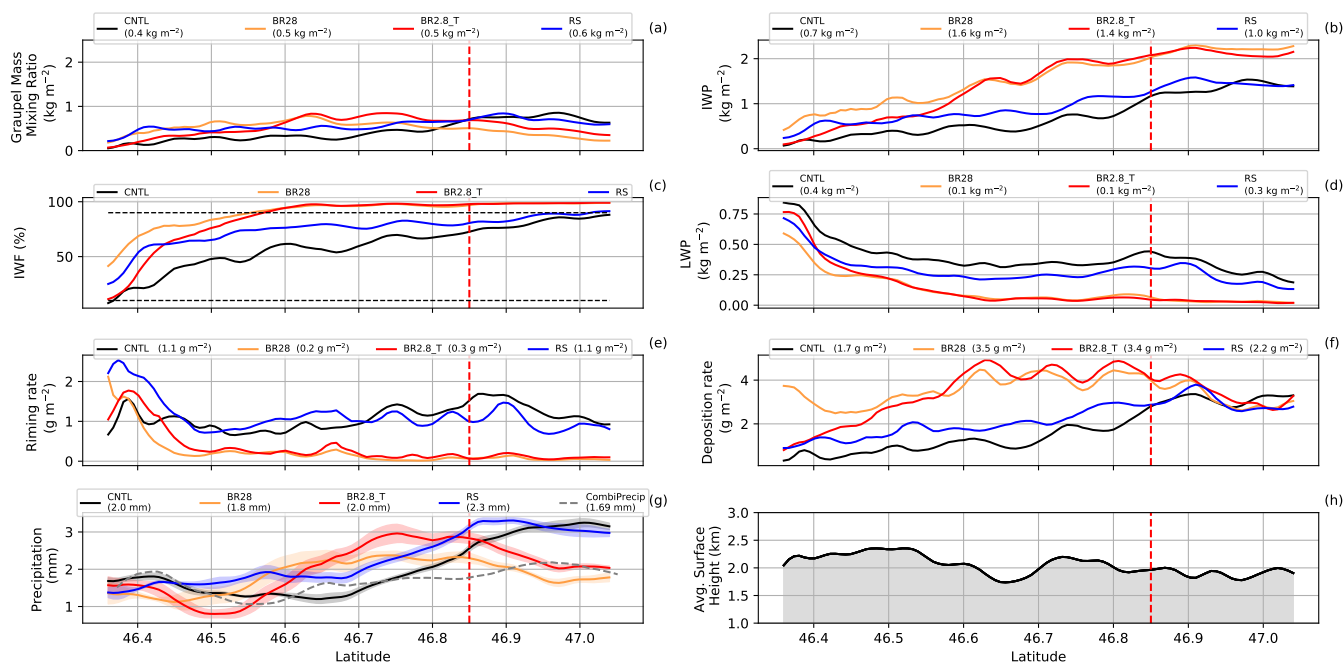
Figure 11. a) Graupel mass concentration, b) IWP, c) IWF (IWP/(IWP + LWP))×100, d) LWP, e) riming rate, f) deposition rate over the cross-section. Theses quantities calculated in a) - f) were only over cloudy regions where the cloud area fraction is larger than 0. In brackets are the average over the latitude. g) Is the precipitation mean (solid line), ensemble spread (shaded area) and CombiPrecip (dashed line) and j) the averaged topography over the cross-section. The red vertical dashed line indicates the latitude of Gotschnagrad

5 Conclusions

Simulations of a cold front passage on 7 March 2019, during the RACLETS campaign in February and March 2019, are carried out with a non-hydrostatic limited-area atmospheric model, COSMO, that uses a two-moment cloud microphysics scheme with six hydrometeor categories. Two parameterizations, droplet shattering upon freezing and collisional breakup that occurs through ice-ice collisions, were additionally added to the already existing Hallett-Mossop parameterization (e.g. Sullivan et al., 2018a; Sotiropoulou et al., 2020). The simplified temperature-dependent collisional breakup parameterization is based on the work of Takahashi et al. (1995) and used here with different configurations of F_{BR} and γ_{BR} to account for the hydrometeor size scaling.

To conclude, our main findings can be summarised as follows:

– Droplet shattering did not show significant differences to the CNTL simulation. This is mainly due to the low raindrop number concentration present during the cold front passage over Gotschnagrat. Aside from using a shattering probability of 10 %, which is similar to Sullivan et al. (2018a), freezing raindrops in COSMO are spectrally partitioned into ice

crystals, snow and graupel and only the partitioned ice crystals are subject to shatter which lowers the likelihood that this SIP proceeds (Blahak, 2008).

– Both the CNTL and rime splintering simulations were not able to capture the ICNC observations at Gotschnagrat. The ice crystals that formed via the primary ice processes above 3 km were mostly converted to snow and graupel reducing the ICNC at the surface. Secondarily formed ice crystals through rime splintering was at most $0.9\,\text{L}^{-1}$ at 3 km and decrease significantly below 3 km. The fact that small concentrations, less than $0.5\,\text{mg}\,\text{m}^{-3}$, of raindrops between 100 and 150 μm were available in the rime splintering region and that Gotschnagrat was not in the rime splintering temperature regime on 7 March limited the rime splintering process. At Davos Wolfgang, all the simulations could not adequately represent the radar precipitation.

– The BR28 and BR2.8_T simulations showed enhanced ICNC at the surface compared to the CNTL simulations and represented the observed ICNC at Gotschnagrat very well. The enhanced SIP production did impact the cloud liquid water, reducing the LWP significantly through the cloud layer and underestimating the LWC at Davos Wolfgang. A 700 m shallow layer of cloud liquid water near the surface was maintained causing cloud droplets and raindrops to rime onto the ice crystals corresponding to rime fractions of less than 5.4 %). However, this could not explain the HoloGondel observations showing that over 50 % of the ice crystals were rimed.

– Including collisional breakup showed to be beneficial for simulating precipitation over the domain. The simulations presenting the stronger SIP, BR28, showed the most improvement in timing and amount of surface precipitation during 7 March. Regions of invigorated precipitations in the CNTL and rime splintering simulations generally were more suppressed when the secondary ice parameterizations were used bringing the precipitations rates closer to the observations.

6 Data availability

The COSMO model output, and the CombiPrecip and HoloGondel observational datasets used for our analysis are available at https://doi.org/10.5281/zenodo.4311567 and the software to analyze the data can be found at https://doi.org/10.5281/zenodo.4316923. The data for the supplementary information are available at https://doi.org/10.5281/zenodo.4316877.

Author contributions. ZD conducted the simulations, analyzed the results, and was the main author of the paper. AL conducted and interpreted the data on the Gotschnabahn. UL and SF contributed to the design of the study and the analysis of the results. All authors contributed to the writing of the study.

Competing interests. The authors declare that they have no conflict of interest.

Acknowledgements. All simulations were performed with the Consortium for Small-scale Modeling (COSMO) model. We thank Sylvia

440   Sullivan for providing the code for secondary ice parameterizations and open communication regarding the model and the parameterizations. The simulations were performed and are stored at the Swiss National Supercomputing Center (CSCS) under project s1009. The authors would like to thank the RACLETS team for the successful measurement campaign and the fruitful scientific discussions. We would also like to especially thank Jörg Wieder for providing the aerosol measurements and Patric Seifert (TROPOS, Germany) for the distrometer and microwave radiometer data, Cyril Brunner and Nadine Borduas-Dedekind for scientific discussions and support. Thanks to MeteoSwiss for

445   providing the CombiPrecip data. ZD, AL and UL acknowledge funding from the Swiss National Science Foundation (SNSF) grant number 200021_175824.

References

Baldauf, M., Seifert, A., Förstner, J., Majewski, D., Raschendorfer, M., and Reinhardt, T.: Operational Convective-Scale Numerical Weather Prediction with the COSMO Model: Description and Sensitivities, Monthly Weather Review, 139, 3887–3905, https://doi.org/10.1175/MWR-D-10-05013.1, 2011.

Beck, A., Henneberger, J., Schöpfer, S., Fugal, J., and Lohmann, U.: HoloGondel: in situ cloud observations on a cable car in the Swiss Alps using a holographic imager, Atmospheric Measurement Techniques, 10, 459–476, https://doi.org/10.5194/amt-10-459-2017, 2017.

Beck, A., Henneberger, J., Fugal, J. P., David, R. O., Lacher, L., and Lohmann, U.: Impact of surface and near-surface processes on ice crystal concentrations measured at mountain-top research stations, Atmospheric Chemistry and Physics, 18, 8909–8927, https://doi.org/10.5194/acp-18-8909-2018, 2018.

Bergeron, T.: On the low-level redistribution of atmospheric water caused by orography., In Proceedings of the International Conference on Cloud Physics, Tokyo, pp. 96–100, 1965.

Blahak, U.: Towards a better representation of high density ice particles in a state-of-the-art two-moment bulk microphysical scheme, p. 9, https://pdfs.semanticscholar.org/9f09/aba324e82fd3129770e84ba47e8c33623380.pdf, 2008.

Blyth, A. M. and Latham, J.: A multi-thermal model of cumulus glaciation via the hallett-Mossop process, Quarterly Journal of the Royal Meteorological Society, 123, 1185–1198, https://doi.org/10.1002/qj.49712354104, 1997.

Bühl, J., Seifert, P., Myagkov, A., and Ansmann, A.: Measuring ice- and liquid-water properties in mixed-phase cloud layers at the Leipzig Cloudnet station, Atmospheric Chemistry and Physics, 16, 10 609–10 620, https://doi.org/10.5194/acp-16-10609-2016, 2016.

Craig, G. C. and Dörnbrack, A.: Entrainment in Cumulus Clouds: What Resolution is Cloud-Resolving?, Journal of the Atmospheric Sciences, 65, 3978–3988, https://doi.org/10.1175/2008JAS2613.1, 2008.

Crosier, J., Choularton, T. W., Westbrook, C. D., Blyth, A. M., Bower, K. N., Connolly, P. J., Dearden, C., Gallagher, M. W., Cui, Z., and Nicol, J. C.: Microphysical properties of cold frontal rainbands†, Quarterly Journal of the Royal Meteorological Society, 140, 1257–1268, https://doi.org/10.1002/qj.2206, 2014.

DeMott, P. J., Prenni, A. J., Liu, X., Kreidenweis, S. M., Petters, M. D., Twohy, C. H., Richardson, M. S., Eidhammer, T., and Rogers, D. C.: Predicting global atmospheric ice nuclei distributions and their impacts on climate, Proceedings of the National Academy of Sciences, 107, 11 217–11 222, https://doi.org/10.1073/pnas.0910818107, 2010.

DeMott, P. J., Prenni, A. J., McMeeking, G. R., Sullivan, R. C., Petters, M. D., Tobo, Y., Niemand, M., Möhler, O., Snider, J. R., Wang, Z., and Kreidenweis, S. M.: Integrating laboratory and field data to quantify the immersion freezing ice nucleation activity of mineral dust particles, Atmospheric Chemistry and Physics, 15, https://doi.org/10.5194/acp-15-393-2015, 2015.

Dong, Y. Y. and Hallett, J.: Droplet accretion during rime growth and the formation of secondary ice crystals, Quarterly Journal of the Royal Meteorological Society, 115, 127–142, https://doi.org/10.1002/qj.49711548507, 1989.

Eirund, G. K., Lohmann, U., and Possner, A.: Cloud Ice Processes Enhance Spatial Scales of Organization in Arctic Stratocumulus, Geophysical Research Letters, 46, 14 109–14 117, https://doi.org/10.3929/ethz-b-000384642, 2019a.

Eirund, G. K., Possner, A., and Lohmann, U.: Response of Arctic mixed-phase clouds to aerosol perturbations under different surface forcings, Atmospheric Chemistry and Physics, 19, 9847–9864, https://doi.org/10.5194/acp-19-9847-2019, 2019b.

Farrington, R. J., Connolly, P. J., Lloyd, G., Bower, K. N., Flynn, M. J., Gallagher, M. W., Field, P. R., Dearden, C., and Choularton, T. W.: Comparing model and measured ice crystal concentrations in orographic clouds during the INUPIAQ campaign, Atmospheric Chemistry and Physics, 16, 4945–4966, https://doi.org/10.5194/acp-16-4945-2016, 2016.

Field, P. R., Lawson, R. P., Brown, P. R. A., Lloyd, G., Westbrook, C., Moisseev, D., Miltenberger, A., Nenes, A., Blyth, A., Choular-
ton, T., Connolly, P., Buehl, J., Crosier, J., Cui, Z., Dearden, C., DeMott, P., Flossmann, A., Heymsfield, A., Huang, Y., Kalesse, H.,
Kanji, Z. A., Korolev, A., Kirchgaessner, A., Lasher-Trapp, S., Leisner, T., McFarquhar, G., Phillips, V., Stith, J., and Sullivan, S.: Sec-
ondary Ice Production: Current State of the Science and Recommendations for the Future, Meteorological Monographs, 58, 7.1–7.20,
https://doi.org/10.1175/AMSMONOGRAPHS-D-16-0014.1, 2016.

Findeisen, W., Volken, E., Giesche, A. M., and Brönnimann, S.: Colloidal meteorological processes in the formation of precipitation, Mete-
orologische Zeitschrift, pp. 443–454, https://doi.org/10.1127/metz/2015/0675, 2015.

Griggs, D. J. and Choularton, T. W.: Freezing modes of riming droplets with application to ice splinter production, Quarterly Journal of the
Royal Meteorological Society, 109, 243–253, https://doi.org/10.1002/qj.49710945912, 1983.

Hallett, J. and Mossop, S. C.: Production of secondary ice particles during the riming process, Nature, 249, 26–28,
https://doi.org/10.1038/249026a0, 1974.

Henneberg, O., Henneberger, J., and Lohmann, U.: Formation and Development of Orographic Mixed-Phase Clouds, Journal of the Atmo-
spheric Sciences, 74, 3703–3724, https://doi.org/10.1175/JAS-D-16-0348.1, 2017.

Henneberger, J., Fugal, J. P., Stetzer, O., and Lohmann, U.: HOLIMO II: a digital holographic instrument for ground-based
in situ observations of microphysical properties of mixed-phase clouds, Atmospheric Measurement Techniques, 6, 2975–2987,
https://doi.org/10.5194/amt-6-2975-2013, 2013.

Heymsfield, A. J., Schmitt, C., Chen, C.-C.-J., Bansemer, A., Gettelman, A., Field, P. R., and Liu, C.: Contributions of the Liquid and Ice
Phases to Global Surface Precipitation: Observations and Global Climate Modeling, Journal of the Atmospheric Sciences, 77, 2629–2648,
https://doi.org/10.1175/JAS-D-19-0352.1, 2020.

Hoarau, T., Pinty, J.-P., and Barthe, C.: A representation of the collisional ice break-up process in the two-moment microphysics LIMA v1.0
scheme of Meso-NH, Geoscientific Model Development, 11, 4269–4289, https://doi.org/10.5194/gmd-11-4269-2018, 2018.

Keil, C., Baur, F., Bachmann, K., Rasp, S., Schneider, L., and Barthlott, C.: Relative contribution of soil moisture, boundary-layer and
microphysical perturbations on convective predictability in different weather regimes, Quarterly Journal of the Royal Meteorological
Society, 145, 3102–3115, https://doi.org/10.1002/qj.3607, 2019.

Keinert, A., Spannagel, D., Leisner, T., and Kiselev, A.: Secondary Ice Production upon Freezing of Freely Falling Drizzle Droplets, Journal
of the Atmospheric Sciences, 77, 2959–2967, https://doi.org/10.1175/JAS-D-20-0081.1, 2020.

Kolomeychuk, R. J., McKay, D. C., and Iribarne, J. V.: The Fragmentation and Electrification of Freezing Drops, Journal of the Atmospheric
Sciences, 32, 974–979, https://doi.org/10.1175/1520-0469(1975)032<0974:TFAEOF>2.0.CO;2, 1975.

Korolev, A.: Limitations of the Wegener–Bergeron–Findeisen Mechanism in the Evolution of Mixed-Phase Clouds, Journal of the Atmo-
spheric Sciences, 64, 3372–3375, https://doi.org/10.1175/JAS4035.1, 2007.

Korolev, A. and Isaac, G.: Phase transformation of mixed-phase clouds, Quarterly Journal of the Royal Meteorological Society, 129, 19–38,
https://doi.org/10.1256/qj.01.203, 2002.

Korolev, A., Heckman, I., Wolde, M., Ackerman, A. S., Fridlind, A. M., Ladino, L. A., Lawson, R. P., Milbrandt, J., and Williams, E.: A
new look at the environmental conditions favorable to secondary ice production, Atmospheric Chemistry and Physics, 20, 1391–1429,
https://doi.org/10.5194/acp-20-1391-2020, 2020.

Korolev, A. V. and Mazin, I. P.: Supersaturation of Water Vapor in Clouds, Journal of the Atmospheric Sciences, 60, 2957–2974,
https://doi.org/10.1175/1520-0469(2003)060<2957:SOWVIC>2.0.CO;2, 2003.

Lauber, A., Kiselev, A., Pander, T., Handmann, P., and Leisner, T.: Secondary Ice Formation during Freezing of Levitated Droplets, Journal of the Atmospheric Sciences, 75, 2815–2826, https://doi.org/10.1175/JAS-D-18-0052.1, 2018.

Lauber, A., Henneberger, J., Mignani, C., Ramelli, F., Pasquier, J. T., Wieder, J., Hervo, M., and Lohmann, U.: Continuous secondary ice production initiated by updrafts through the melting layer in mountainous regions, Atmospheric Chemistry and Physics Discussions, pp. 1–26, https://doi.org/10.5194/acp-2020-986, 2020.

Leisner, T., Pander, T., Handmann, P., and Kiselev, A.: Secondary ice processes upon heterogeneous freezing of cloud droplets, AMS, 2014.

Lloyd, G., Choularton, T. W., Bower, K. N., Gallagher, M. W., Connolly, P. J., Flynn, M., Farrington, R., Crosier, J., Schlenczek, O., Fugal, J., and Henneberger, J.: The origins of ice crystals measured in mixed-phase clouds at the high-alpine site Jungfraujoch, Atmospheric Chemistry and Physics, 15, 12 953–12 969, https://doi.org/10.5194/acp-15-12953-2015, 2015.

Lohmann, U., Henneberger, J., Henneberg, O., Fugal, J. P., Bühl, J., and Kanji, Z. A.: Persistence of orographic mixed-phase clouds, Geophysical Research Letters, 43, 10,512–10,519, https://doi.org/10.1002/2016GL071036, 2016a.

Lohmann, U., Lüönd, F., and Mahrt, F.: An introduction to clouds: From the Microscale to climate, Cambridge University Press, https://doi.org/10.1017/CBO9781139087513, 2016b.

Mellor, G. L. and Yamada, T.: Development of a turbulence closure model for geophysical fluid problems, Reviews of Geophysics, 20, 851–875, https://doi.org/https://doi.org/10.1029/RG020i004p00851, 1982.

Milbrandt, J. A. and Morrison, H.: Parameterization of Cloud Microphysics Based on the Prediction of Bulk Ice Particle Properties. Part III: Introduction of Multiple Free Categories, Journal of the Atmospheric Sciences, 73, 975–995, https://doi.org/10.1175/JAS-D-15-0204.1, 2015.

Morrison, H., Boer, G. d., Feingold, G., Harrington, J., Shupe, M. D., and Sulia, K.: Resilience of persistent Arctic mixed-phase clouds, Nature Geoscience, 5, 11–17, https://doi.org/10.1038/ngeo1332, 2012.

Mülmenstädt, J., Sourdeval, O., Delanoë, J., and Quaas, J.: Frequency of occurrence of rain from liquid-, mixed-, and ice-phase clouds derived from A-Train satellite retrievals, Geophysical Research Letters, 42, 6502–6509, https://doi.org/10.1002/2015GL064604, 2015.

Otkin, J., Huang, H.-L., and Seifert, A.: A comparison of microphysical schemes in the WRF model during a severe weather event, Papers del 7th WRF Users' Workshop, Boulder, CO, USA, p. 6, 2006.

Ovtchinnikov, M. and Kogan, Y. L.: An Investigation of Ice Production Mechanisms in Small Cumuliform Clouds Using a 3D Model with Explicit Microphysics. Part I: Model Description, Journal of the Atmospheric Sciences, 57, 2989–3003, https://doi.org/10.1175/1520-0469(2000)057<2989:AIOIPM>2.0.CO;2, 2000.

Panosetti, D., Schlemmer, L., and Schär, C.: Convergence behavior of idealized convection-resolving simulations of summertime deep moist convection over land, Clim Dyn, https://doi.org/10.1007/s00382-018-4229-9, https://doi.org/10.1007/s00382-018-4229-9, 2018.

Phillips, V. T. J., Blyth, A. M., Brown, P. R. A., Choularton, T. W., and Latham, J.: The glaciation of a cumulus cloud over New Mexico, Quarterly Journal of the Royal Meteorological Society, 127, 1513–1534, https://doi.org/10.1002/qj.49712757503, 2006.

Phillips, V. T. J., Yano, J.-I., Formenton, M., Ilotoviz, E., Kanawade, V., Kudzotsa, I., Sun, J., Bansemer, A., Detwiler, A. G., Khan, A., and Tessendorf, S. A.: Ice Multiplication by Breakup in Ice–Ice Collisions. Part II: Numerical Simulations, Journal of the Atmospheric Sciences, 74, 2789–2811, https://doi.org/10.1175/JAS-D-16-0223.1, 2017.

Possner, A., Ekman, A. M. L., and Lohmann, U.: Cloud response and feedback processes in stratiform mixed-phase clouds perturbed by ship exhaust, Geophysical Research Letters, 44, 1964–1972, https://doi.org/10.1002/2016GL071358, 2017.

Ramelli, F., Henneberger, J., David, R. O., Lauber, A., Pasquier, J. T., Wieder, J., Bühl, J., Seifert, P., Engelmann, R., Hervo, M., and Lohmann, U.: Influence of low-level blocking and turbulence on the microphysics of a mixed-phase cloud in an inner-Alpine valley, Atmospheric Chemistry and Physics Discussions, pp. 1–29, https://doi.org/10.5194/acp-2020-774, 2020.

560 Rogers, D. C. and Vali, G.: Ice Crystal Production by Mountain Surfaces, Journal of Climate and applied Meteorology, 26, 1152–1168, https://doi.org/10.1175/1520-0450(1987)026<1152:ICPBMS>2.0.CO;2, 1987.

Rotach, M. W. and Zardi, D.: On the boundary-layer structure over highly complex terrain: Key findings from MAP, Quarterly Journal of the Royal Meteorological Society, 133, 937–948, https://doi.org/https://doi.org/10.1002/qj.71, 2007.

Schär, C., Leuenberger, D., Fuhrer, O., Lüthi, D., and Girard, C.: A New Terrain-Following Vertical Coordinate Formulation for Atmospheric

565 Prediction Models, Monthly Weather Review, 130, 2459–2480, https://doi.org/10.1175/1520-0493(2002)130<2459:ANTFVC>2.0.CO;2, 2002.

Seifert, A. and Beheng, K. D.: A two-moment cloud microphysics parameterization for mixed-phase clouds. Part 1: Model description, Meteorology and Atmospheric Physics, 92, 45–66, https://doi.org/10.1007/s00703-005-0112-4, 2006.

Seifert, P.: LIDAR Davos Wolfgang, EnviDat, https://www.envidat.ch/dataset/lidar-davos-wolfgang, 2019.

570 Selz, T. and Craig, G. C.: Upscale Error Growth in a High-Resolution Simulation of a Summertime Weather Event over Europe, Monthly Weather Review, 143, 813–827, https://doi.org/10.1175/MWR-D-14-00140.1, 2015.

Sideris, S. V., Gabella, M., Sassi, M., and Germann, U.: The CombiPrecip experience: development and operation of a real-time radar-raingauge combination scheme in Switzerland, p. 10, Washington DC, USA, 2014.

Sotiropoulou, G., Sullivan, S., Savre, J., Lloyd, G., Lachlan-Cope, T., Ekman, A. M. L., and Nenes, A.: The impact of secondary ice produc-

575 tion on Arctic stratocumulus, Atmospheric Chemistry and Physics, 20, 1301–1316, https://doi.org/10.5194/acp-20-1301-2020, 2020.

Sullivan, S. C., Hoose, C., and Nenes, A.: Investigating the contribution of secondary ice production to in-cloud ice crystal numbers, Journal of Geophysical Research: Atmospheres, 122, 9391–9412, https://doi.org/10.1002/2017JD026546, 2017.

Sullivan, S. C., Barthlott, C., Crosier, J., Zhukov, I., Nenes, A., and Hoose, C.: The effect of secondary ice production parameterization on the simulation of a cold frontal rainband, Atmospheric Chemistry and Physics, 18, 16 461–16 480, https://doi.org/10.5194/acp-18-16461-

580 2018, 2018a.

Sullivan, S. C., Hoose, C., Kiselev, A., Leisner, T., and Nenes, A.: Initiation of secondary ice production in clouds, Atmospheric Chemistry and Physics, 18, 1593–1610, https://doi.org/10.5194/acp-18-1593-2018, 2018b.

Takahashi, T., Nagao, Y., and Kushiyama, Y.: Possible High Ice Particle Production during Graupel–Graupel Collisions, Journal of the Atmospheric Sciences, 52, 4523–4527, https://doi.org/10.1175/1520-0469(1995)052<4523:PHIPPD>2.0.CO;2, 1995.

585 Touloupas, G., Lauber, A., Henneberger, J., Beck, A., and Lucchi, A.: A convolutional neural network for classifying cloud particles recorded by imaging probes, Atmospheric Measurement Techniques, 13, 2219–2239, https://doi.org/10.5194/amt-13-2219-2020, 2020.

Vardiman, L.: The Generation of Secondary Ice Particles in Clouds by Crystal–Crystal Collision, Journal of the Atmospheric Sciences, 35, 2168–2180, https://doi.org/10.1175/1520-0469(1978)035<2168:TGOSIP>2.0.CO;2, 1978.

Wang, P. K.: Diffusion growth and evaporation of cloud and precipitation particles, in: Physics and Dynamics of Clouds and Precipitation,

590 pp. 228–251, Cambridge University Press, Cambridge, https://doi.org/10.1017/CBO9780511794285.010, 2013.

Wegener, A.: Thermodynamik der Atmosphäre., J.A. Barth, Leipzig, 1911.

Wildeman, S., Sterl, S., Sun, C., and Lohse, D.: Fast Dynamics of Water Droplets Freezing from the Outside In, Physical Review Letters, 118, 084 101, https://doi.org/10.1103/PhysRevLett.118.084101, 2017.

Yano, J.-I. and Phillips, V. T. J.: Ice–Ice Collisions: An Ice Multiplication Process in Atmospheric Clouds, Journal of the Atmospheric
595   Sciences, 68, 322–333, https://doi.org/10.1175/2010JAS3607.1, 2010a.

Yano, J.-I. and Phillips, V. T. J.: Ice–Ice Collisions: An Ice Multiplication Process in Atmospheric Clouds, Journal of the Atmospheric
     Sciences, 68, 322–333, https://doi.org/10.1175/2010JAS3607.1, 2010b.

Yano, J.-I., Phillips, V. T. J., and Kanawade, V.: Explosive ice multiplication by mechanical break-up in ice–ice collisions: a dynamical
     system-based study, Quarterly Journal of the Royal Meteorological Society, 142, 867–879, https://doi.org/10.1002/qj.2687, 2016.

600   Young, G., Lachlan-Cope, T., O'Shea, S. J., Dearden, C., Listowski, C., Bower, K. N., Choularton, T. W., and Gallagher, M. W.:
     Radiative Effects of Secondary Ice Enhancement in Coastal Antarctic Clouds, Geophysical Research Letters, 46, 2312–2321,
     https://doi.org/10.1029/2018GL080551, 2019.